Nanoporous Iridium Nanosheets for Polymer Electrolyte Membrane (PEM) Electrolysis

Swarnendu Chatterjee^{1, ‡}, Xiong Peng^{2, ‡}, Saad Intikhab¹, Guosong Zeng³, Nancy N. Kariuki⁴, Deborah J. Myers⁴, Nemanja Danilovic^{2*}, Joshua Snyder^{1*}

Corresponding Authors: jds43@drexel.edu, ndanilovic@lbl.gov

Abstract

Growth of the hydrogen economy is predicated on advancements in electrochemical energy technologies, with water electrolysis as a key component to the technological portfolio. Much of the focus on anode catalyst development for polymer electrolyte membrane water electrolyzers (PEMWE) is centered on activity as controlled by compositional and morphological impacts on reactant/intermediate/product adsorption. However, the effectiveness of this strategy is found to be limited upon integration of these materials into PEMWE membrane electrode assemblies (MEA). Regardless of catalyst activity, the combination of electrode inhomogeneity, ionomer integration, and high density of oxide-oxide interfaces yield significant performance losses associated with poor catalytic electrode conductivity. Here we address many of these limitations through the development of a unique catalyst morphology composed of nanoporous Ir nanosheets (npIr_x-NS) that exhibit high catalytic activity for the anodic oxygen evolution reaction (OER) and superior electrode electronic conductivity in comparison to a commercial IrO₂ nanoparticle catalyst. The utility of the npIr_x-NS is demonstrated through incorporation into PEMWE MEAs where their performance exceeds that of commercial catalyst coated membranes (CCM) at loadings as low as 0.06 mg_{Ir} cm⁻² while exhibiting a negligible loss in performance following 50,000 accelerated stress test cycles.

¹ Department of Chemical and Biological Engineering, Drexel University, Philadelphia, PA, 19104, USA

² Energy Storage and Distributed Resources Division, Lawrence Berkeley National Laboratory, Berkeley, California 94720, USA

³ Chemical Science Division, Lawrence Berkeley National Laboratory, Berkeley, California 94720, USA

⁴ Chemical Sciences and Engineering Division, Argonne National Laboratory, Lemont, IL, 60439, USA

[¥] These authors contributed equally

Introduction

A central focus of deep decarbonization of the energy sector is realization of the hydrogen economy and renewable electricity generation¹. Recent emphasis on water electrolysis for hydrogen production in both Europe and the US has brought this technology into the spotlight as a means for achieving a hydrogen economy^{2–4}. Proton exchange membrane water electrolyzers (PEMWE) are emerging as the preferred technology to interface with intermittent renewable electricity due to multiple advantages afforded by the solid polymer membrane, over the incumbent alkaline water electrolysis, including: high turndown ratio, differential H₂ pressure generation, and high current densities decreasing the system footprint significantly^{5,6}. As with all developing renewable energy technologies, political, regulatory, and technological barriers impede broad market integration for PEM electrolysis. Surpassing these barriers with innovative technological advances will help to hasten the hydrogen age.

Commercial integration requires not only operational efficiency but also longevity. In the breadth of oxygen evolving electrocatalysts currently available, Ir and its derived oxides are the only viable materials to meet both activity and durability needs^{7–11}. The standard ionomer agglomerated form factor for PEMWE anode catalyst layers^{5,6,12} is severely limited by the high density of oxide-oxide interfaces established between catalyst particles that populate the pathway from catalytic site to current collector. This results in a higher in-plane and through-plane resistivity compared to fuel cell catalyst layers employing carbon supported Pt¹³. Full realization of the importance of electronic conductivity, distinctly different from protonic conductivity, in influencing current distributions, reaction overpotentials, and overall PEMWE stack efficiency has only recently started to receive sufficient attention^{13–15}. Efficiency losses are exacerbated as anode catalyst loading decreases and ionomer:catalyst ratios are shifted to improve protonic conductivity through the electrode^{13–15}. Current strategies to mitigate resistive losses in oxide-based catalyst

layers include: refining catalyst morphology to improve both utilization and inter-particle contact and contact with the gas diffusion media^{6,15,16}, inclusion of microporous layers to improve contact between the gas diffusion media and the catalyst layer^{5,9,12,13}, addition of supporting materials to improve electrical contact and lower resistivity throughout the catalyst layer^{14,19,20}, etc.

Recent work on bicontinuous materials, namely nanoporous metals, have shown that the combination of the high surface-to-volume ratio, consequent high electrochemically active surface area (ECSA), and a continuous metallic backbone, result in high mass normalized activity and low electrode resistivity^{21–25}. Utility of this anode electrocatalyst architecture is currently limited, due to issues associated with direct integration of nanoporous metals into PEMWE catalyst layers. The challenges with this morphology include mechanical instability, nanoporous metals are brittle^{26,27}, and the impact of nanoporosity tortuosity on water and gas transport, limiting catalyst utilization. This issue will be exacerbated with increasing depth of nanoporosity. Here we have developed a unique top-down synthesis protocol for the manufacture of nanoporous nanosheets of Ir (npIr_x-NS). With this material, we get the benefits of nanoporous metals, namely the high electrochemically active surface area (ECSA) per mass and bicontinuous metallic backbone for high in-plane/through-plane conductivity, while producing it in a form factor that can be readily incorporated into PEMWE membrane electrode assemblies (MEA) through existing ink processing techniques. These nanosheets show enhanced performance to the state-of-the-art commercial Ir-based OER electrocatalysts (TKK IrO₂) with reduced ohmic losses and exceptional durability after 50,000 accelerated durability cycles in the PEMWE MEA.

Experimental

Synthesis of npIrx-NS

Nanoporous iridium nanosheets (npIr_x-NS) are prepared by electrochemical dealloying of $Ni_{(100-x)}Ir_x$ (x ≤ 10 at.%) alloy foils. Alloys are formed from high purity precursor metals (Ni pellets from Kurt J Lesker, purity above 99.9% and Ir pellets from Goodfellow, purity 99.9%) in a radio frequency induction furnace (Ambrell EasyHeat 3542 LI) under Ar gas. The synthesized alloys are rolled into thin ribbons using a rolling mill. Intermittent annealing under Ar is used during the rolling process to remove work hardening and promote homogenization of the precursor alloys. The final thickness of the $Ni_{(100-x)}Ir_x$ precursor alloy ribbons is $\sim 100 \mu m$. The npIr_x-NS are obtained by electrochemically dealloying (three electrode cell with Toray carbon paper counter electrode and Ag/AgCl (BASi) reference electrode) of Ni_(100-x)Ir_x precursor alloys in electrolytes composed of a mixture of HCl and H₂SO₄ with potential cycling between -0.05 V and 1 V vs. RHE at a scan rate of 50 mV/s. During potentiodynamic dealloying, the npIr_x-NS delaminate from the foil electrode and settle to the bottom of the electrochemical cell. Following dealloying, the npIr_x-NS are collected through centrifugation (1000 rpm for 30 min.) and washed with Millipore water (Milli-Q synthesis A10). The collected catalyst is washed a minimum of three times to remove residual acid.

Material characterization

The structure, surface morphology and elemental composition of npIr_x-NS electrocatalysts are analyzed using scanning electron microscopy (SEM) (Zeiss Supra 50VP), with Oxford UltiMax 40mm energy dispersive spectrometer for elemental analysis, and transmission electron microscopy (TEM) (JEOL JEM2100, 200kV FEI monochromated F20 UT Tecnai). The pristine sample is prepared by dropping ethanol dispersed ink onto a Cu sample holder. The post-tested sample is prepared by a similar process after abrasively removing the anode catalyst layer after 50,000 cycles.

The X-ray scattering data are collected on a combined Bonse-Hart (USAXS) and pinhole (small angle and wide angle X-ray scattering, SAXS/WAXS) instrument at beamline 9-ID-C at the Advanced Photon Source located at Argonne National Laboratory. Details regarding the optics and instrumentation have been previously reported^{28–31}. The X-ray beam is monochromatized via a pair of Si(220) crystals to an energy of 21 keV. The beam spot size for USAXS is 0.8×0.6 mm (horizontal \times vertical) and 0.8×0.2 mm for SAXS and WAXS. The data acquisition times are 90 s for USAXS and 30 s for both SAXS and WAXS. The samples are prepared by transferring the electrode layers from their respective substrates to single-sided, transparent 3M Scotch Magic tape using a press-peel technique. The samples are then supported in a custom-made sample holder for the WAXS/SAXS/USAXS measurements. During data reduction, patterns collected on a blank piece of tape are subtracted from the patterns acquired for the samples. The data are background corrected and reduced with the NIKA software package²⁹, and data analysis is conducted using the IRENA software package³⁰. Both packages are run on IGOR Pro 8.0 (Wavemetrics). Particle size distribution is obtained from the measured scattering data using the maximum entropy (MaxEnt) method³¹, which involves a constrained optimization of parameters to solve the scattering equation:

$$I(q) = \Delta Q |2\int |F(q, r)| 2(V(r)) 2Np(r) dr$$

where, I(q) is the scattered intensity, Q is the scattering length density of the particle, and F(q,r) is the scattering function at scattering vector q of a particle of characteristic dimension r, V is the volume of the particle, and Np is the number density of particles in the scattering volume.

Half-cell OER testing

Catalyst inks for npIr_x-NS and IrO_x (TKK) are prepared in 2-propanol (Sigma-Aldrich, assay: 99.999%) aqueous solution (isopropanol:water = 1:4; v:v) with 1 µL of 5 wt.% Nafion (Ion Power) solution per mL of ink as a binder. Ionomer to catalyst ratio is 0.05. Ink concentration is 1 mg catalyst per mL solvent. The catalyst ink is drop cast on glassy carbon disk (0.196 cm²) with approximate electrocatalyst loadings of 28 µg/cm² and 175 µg/cm² for half-cell OER testing. All half-cell electrochemical experiments are conducted in a three-electrode electrochemical cell using an Autolab PGSTAT128N potentiostat. OER activity is measured in Ar-purged 0.1 M HClO4 (OmniTrace Ultra, Millipore) made with Millipore water. An Ag/AgCl electrode (BASi) is used as the reference electrode with Toray carbon paper as the counter electrode. All the glassware is cleaned in a 1:1 v:v solution of concentrated sulfuric and nitric acid followed by boiling in Millipore water before each use. Roughness factors for the npIr_x-NS is determined capacitively through a procedure outlined in ²⁵.

Catalyst Coated Membrane (CCM) Fabrication and Membrane Electrode Assembly (MEA)
Testing

Anode ink is prepared by mixing the synthesized npIr_x-NS or commercially available TKK with water, ethanol, and n-propanol at a ratio of 1:1:2 by volume, and NafionTM ionomer solution (5 wt%, Ion Power D521). Ionomer to Ir catalyst mass ratio is kept constant at 0.116 in the study. The anode ink is immersed in an ice bath, sealed with parafilm and sonicated using a horn sonicator (CEX500, Cole-Parmer) at 30% of power for 30 min prior to deposition. The cathode ink is prepared by mixing Pt/C (45.6 wt% Pt, Tanaka) with equal parts water and n-propanol, and NafionTM ionomer solution (5 wt%, Ion Power D521). The ionomer to carbon mass ratio is kept at 0.6 for cathode ink. The cathode inks are then sonicated at constant temperature of 10 °C in a bath sonicator for 30 minutes prior to deposition. The inks are prepared immediately prior to being

spray-deposited onto NafionTM N117 membranes using a Sono-Tek ultrasonic spray coater. The NafionTM perfluorosulfonic acid membranes (N117, Ion Power) are prepared by soaking in DI water at 90 °C for one hour followed by immersion in 0.5 M HNO₃ (ACS Reagent, Sigma-Aldrich) for one hour at room temperature to remove impurities and protonate the sulfonic-acid groups. Finally, the treated membranes are rinsed three times using DI water to remove excess acid and stored in DI water until catalyst coating is performed. The Sono-Tek sonication is set to 120 kHz, and the spray deck, consisting of a porous aluminum plate and vacuum pump, holds the membrane in place. The spray deck is held constant at 80 °C. The cathode and anode deposition process are similar, with spray passes held constant where possible. After spray coating, the precious metal loading is measured using X-ray fluorescence (XRF) (Bruker M4 Tornado). The XRF is calibrated using commercial standards (Micromatter Technologies Inc) to ensure accuracy at low Ir loadings⁶.

Cell Assembly. CCMs with 5 cm² active area are assembled in single cell hardware (Fuel Cell Technology) with a graphite single channel serpentine flow field on cathode and platinized titanium parallel flow field on anode. The CCM is rehydrated at room temperature in DI water before it is assembled into the cell. Teflon gaskets are used on both anode and cathode. Carbon paper without a microporous layer (Toray 120) is used as cathode gas diffusion layers (GDL). Platinized sintered titanium (obtained from Proton OnSite/NEL) is used as the anode poroustransport layers (PTLs). The appropriate thickness PTFE (McMaster-Carr) gaskets are used to obtain 30% compression in the GDLs, while a thickness-matched gasket is used for the Ti-PTL. A torque of 4.5 Nm is applied to the cell to ensure proper sealing.

Cell Testing. A multichannel potentiostat (VSP300, Biologic) equipped with electrochemical impedance spectroscopy (EIS) and a 20 A booster is used for all full-cell electrochemical tests.

The test station used is a modified Fuel Cell Technology (FCT) test stand; the modification is an addition of a water recirculation system for electrolysis testing. Before any electrochemical testing, hot DI water is supplied at 80 °C on the anode side to preheat the cell for 30 min, after which, an auxiliary heater is used to further heat up the cell to 80 °C. Temperature uniformity across the cell is verified with an IR camera. 100 mL min⁻¹ of H₂ is supplied to the cathode at ambient pressure to ensure a pseudo-steady reference electrode for electrolyzer operation. Conditioned cyclic voltammetry (CV) is taken by scanning between 1.2 and 2.0 V at 50 mV s⁻¹ for 10 cycles before recording polarization curves and electrochemical impedance. The polarization curve is taken by holding at various constant cell currents for 130 s while recording cell voltage. The last five voltage data points recorded are averaged and plotted at the corresponding current. The impedance is measured in a galvanostatic mode by applying an AC current perturbation between 200 kHz - 100 mHz to the cell and measuring its voltage response at each polarization step. The amplitude of the AC current is chosen for each step to obtain a sufficient signal to noise ratio, while keeping the perturbation small enough to ensure a linear system response. The npIr_x-NS cyclic voltammetry is measured at various scan rates by cycling the electrode from 0.05 - 1.2 V at 50 mV $\rm s^{\text{--}1}$ at 80 $^{\circ} C$ with DI water and H₂ fed to anode and cathode, respectively.

The accelerated stress testing (AST) cycles are conducted by cycling the anode from either 1.3 - 2.0 V or 1.3 - 1.8 V depending on the Ir loading. During AST, cell temperature is kept at 80 °C while hot water and H₂ gas are fed to anode and cathode, respectively.

Overpotential analysis. The cell voltage E_{cell} is composed of the sum of the reversible cell potential E_{rev}^0 and the three main overpotentials η_i :

$$E_{cell} = E_{rev}^{0} + \eta_{kin} + \eta_{\Omega} + \eta_{mt}$$
 Equation 1

where η_{kin} is the kinetic, η_{Ω} the ohmic, and η_{mt} the mass transport overpotential. Since HER is more favourable in kinetics and mass transport under current testing conditions compared to OER, the overpotential analysis only considers the OER side.

At a temperature of 80 °C, the saturation pressure of H₂O is 0.47 bar_a. For liquid water, the activity of water, $a(H_2O)$, is one, while the activity of the gaseous species is represented by the ratio of their partial pressure to the standard pressure of 1 bar. The temperature dependent standard reversible potential, E_{rev}^0 , can be obtained from the literature ³²

$$E_{rev}^0 = 1.2291 - 0.0008456 \cdot (T - 298.15)$$
 Equation 2

where the voltages, first two terms on right hand side of equation, are measured in V, and the temperatures in K. Under current electrolyzer testing conditions, the E_{rev}^0 is calculated to be 1.168 V, with a thermoneutral voltage of 1.42 V.

Ohmic overpotential η_{Ω} . EIS is used to measure the high frequency resistance (HFR) representing the total electronic cell resistance R_{tot} . The ohmic overpotential, η_{Ω} , is therefore determined as:

$$\eta_{\Omega} = i * R_{tot} = i * HFR$$
 Equation 3

Kinetics overpotential η_{kin} . The kinetic overpotential is extracted using a Tafel model, in which the Tafel slope b and exchange current density i_0 are the governing kinetic parameters. The Tafel model was fitted to iR-free PEMWE cell voltages between 4 and 20 mA/cm². Assuming a non-polarizable HER, the entire kinetic overpotential of the cell is governed by OER with the Tafel slope b as 2.303*RT/4F where R is the ideal gas constant, T is temperature, and F is Faraday's constant:

$$\eta_{kin} = b * log\left(\frac{i}{i_0}\right)$$
 Equation 4

Mass transport overpotential η_{mt} . The mass transport is a summary of gaseous/liquid transfer in the PTL/CL and ionic transport in the CLs. In this study, it is calculated by subtracting the reversible cell potential and kinetic and ohmic overpotentials from the measured cell potential.

Results and Discussion

The critical deficiency of the standard Ir-black or IrO₂-based nanoparticle catalyst architecture is the low in-plane and through-plane conductivity, which results in ohmic and kinetic losses due to under-utilization of active sites, particularly at high current densities (HCD). Key to mitigating these inefficiencies is a catalyst layer morphology/design that minimizes the density of oxide-oxide interfaces established between catalyst particles and maximizes in-plane and through-plane low resistivity pathways to maximize catalyst utilization. To this end, presented here is a catalyst morphology that is composed of nanosheets of nanoporous Ir (npIr_x-NS), **Figure 1(a)** and **1(b)**. The nominal lateral dimension of these nanosheets is on the order of 1 micron while their thickness is on the order of 100 nm with a porosity feature size down to ~5 nm. As schematically represented in **Figure 1(c)**, the lateral span of the nanosheets and their layered morphology, in addition to the bicontinuous metallic backbone that makes up the nanoporous nanosheet architecture, creates low resistivity pathways for electron conduction^{22,25}. This can partially compensate for the suboptimal contact between the gas diffusion electrode and the catalyst layer^{33,34}, **Figure 1(c)**.

There is some literature precedence for the design of nanoporous metals formed through dealloying multicomponent alloys for use as OER electrocatalysts^{21–25}. Dealloying is defined as the selective chemical/electrochemical etching of a sacrificial component(s) from a multicomponent alloy, evolving an open, bicontinuous, high aspect ratio nanoporousity^{35–37}. The specific utility of nanoporous metals for catalyzing the OER is their nanostructured morphology

yielding a highly defected catalyst surface^{22,38,39}, a high surface area-to-volume ratio to maximize precious metal utilization, and high electronic conductivity due to an interconnected metallic backbone^{22,25}. While promising results have been shown in the half-cell^{21–25}, the standard morphology of these nanoporous catalysts is that of a thin film. This type of morphology cannot be readily incorporated into the anode catalyst layer of PEMWE MEAs. Additionally, thick nanoporous layers with small, tortuous porosity will result in under-utilization of catalyst as the OER on much of the surface will be limited by reactant/product transport⁴⁰. Many of the limitations associated with the nanoporous catalyst morphology are alleviated through the npIr_x-NS catalyst developed here.

The limited literature precedence for nanoporous Ir formed through dealloying^{21,22,25} is a consequence of the unique challenges that are a result of the specific properties of Ir. Ir is a slow diffusing species, surface diffusivities roughly scale with melting point⁴¹, and has a propensity to form a stable oxide at anodic potentials. Nanoporosity evolution through dealloying is defined by a competition between dissolution and surface diffusion where corrosion of the sacrificial component is followed by dynamic rearrangement of the surface to form the nanoporous backbone. This process can be limited by slow diffusing metals such as Ir. The layer-by-layer etch front propagation can be stymied through surface passivation by the slow-moving species, even with sufficient less noble component percolation throughout the alloy. To prevent surface passivation and promote etch front propagation we use electrolyte additives. The goal here is to enhance rates of Ir surface diffusion^{42–44}, increase the corrosion rate of the sacrificial component (Ni in this work), and limit or disrupt the formation of Ir oxide to some extent. We note here that Ni is meant to just be a sacrificial element to aid the formation of nanoporosity. We do not expect or target any impact of Ni, electronic or otherwise, on the OER activity as the residual Ni content following

dealloying is < 10 at.%. Adding chloride ions (~500 mM) in 2 M H₂SO₄ and maintaining a high sacrificial component content, > 90 at.% Ni in this case, results in bicontinuous nanoporosity, Figure 1(a), 1(b), 2(c), 2(d), and S2. The anodic curves for potentiodynamic dealloying (cycling between -0.05 V and 1 V vs. RHE) for a range of Ni_(100-x)Ir_x compositions are shown in Figure 2(a). The critical potential for initiating dealloying increases with Ir content while the peak Ni dissolution current decreases with increasing Ir content, as is expected from observations of more traditional dealloying systems such as AgAu³⁵⁻³⁷. Ni dissolution currents, increasing with increasing potential, eventually decrease as the surface becomes passivated in a stable Ir oxide^{45,46}. Ni etching continues following reduction of the surface Ir during the cathodic sweep. A simple survey of precursor alloy composition and Cl⁻ content in the electrolyte shows that the npIr_x-NS thickness is a weak function of alloy composition and a relatively strong function of Cl⁻ electrolyte content, Figure 2(b). Systematic variation of the dealloying conditions finds that nanoporous nanosheet exfoliation from precursor NiIr foils only occurs for low Ir content, < 10 at.%, and Cl⁻ concentrations ≥ 100 mM, Figure S2. The distinct mechanism for the formation and exfoliation of these nanosheets remains to be determined. However, this processing methodology is reproducible and is amenable to the synthesis of gram-scale quantities of nanoporous catalyst material.

The npIr_x-NS formed from the Ni₉₅Ir₅ precursor alloy have been selected as the representative material for both half-cell and MEA testing as they exhibit the best combination of material homogeneity and performance. One of the challenges with 2D materials is loading-dependent aggregation, forming a layer-by-layer morphology which can act to inhibit reactant/product transport through the catalyst layer, essentially deactivating a significant mass of the material. This is in contrast to nanoparticulate based catalysts where particle aggregation,

especially in the presence of supports, results in multi-scale porosity^{47,48}. Thus, there is a tradeoff between increasing electronic transport and reaction turnover that comes with higher mass loadings and decreasing catalyst utilization percentages and deteriorating mass transport. The advantage of the 2D npIr_x-NS morphology is that they are also nanoporous. Therefore, even if the 2D sheets aggregate, there is still a viable pathway for reactants/products to move through the catalyst layer. Additionally, the minimized thickness (< 100 nm) of the npIr_x-NS limits the underutilization of active area within the tortuous nanoporous architecture, particularly at HCD. For our comparison to commercially available Ir-based electrocatalysts we use TKK IrO2, a state-of-theart electrocatalyst for PEMWE capable of high performance in RDE-based OER testing⁴⁹ and at low loadings in PEMWEs⁶. Figures 3(a), (b), and (c) show that there is no significant difference in OER activity for TKK IrO₂ and npIr_x-NS at two different loadings (28 µg/cm² and 175 µg/cm²). The capacitively-determined roughness factors (RF), Figure 3(c), show an expected increase in RF with loading for both TKK IrO₂ and npIr_x-NS. This is an indication that layering of the 2D nanosheets does not impede access to the catalytic surface throughout the entirety of the catalyst layer. The Tafel slopes for TKK IrO₂ and npIr_x-NS both lie between 50 and 60 mV/dec (54 and 57 mV/dec, respectively), in line with published values for other IrO_x-based catalysts ^{12,49}.

Demonstrating the utility of the nanoporous nanosheets, particularly their impact on interand intra-particle electronic conductivity and the benefits of nanoporosity, we integrate them for the first time into PEMWE MEAs. Two MEAs are prepared using the state-of-the-art non-supported IrO₂ (TKK) and npIr_x-NS at an Ir loading of 0.17 mg_{Ir} cm⁻² in the anode catalyst layer formed through spray deposition⁵⁰. Water electrolysis testing is conducted in a 5 cm² single cell with polarization curves recorded at 80 °C and ambient pressure, **Figure 4(a)**. The npIr_x-NS show a slight improvement over TKK IrO₂ in the kinetic region at low current density while an apparent

higher mass transport resistance is observed at higher current densities as compared to TKK IrO2. Deconvolution of the various contributions to the polarization curves are assessed by a polarization performance voltage breakdown, **Figures 4(b)** to **(d)**. A lower kinetic overpotential of roughly 10 mV at all current densities indicates a higher OER activity for the npIr_x-NS as compared to TKK IrO₂ (Figure 4(b)). Additionally, the npIr_x-NS exhibit a 20 mV smaller ohmic resistance compared to TKK IrO₂ (Figure 4(c)) at 2.4 A/cm². As the total catalyst mass loading as well as the catalystto-ionomer ratio are identical for both anode catalyst layers, the decreased ohmic resistance can be attributed to an increased inter- and intra-particle conductivity. This is a consequence of the reduction of oxide-oxide interfaces and the metallic backbone of the high aspect ratio nanosheets and their lateral geometry, improving contact between the catalyst layer and the gas diffusion media, even at low loadings (see schematic in Figure 1). The decrease in the HCD performance for the npIr_x-NS, Figure 4(a), can be directly attributed a higher mass transport resistance of roughly 125 mV (at 2.4 A/cm²) in comparison to TKK IrO₂, Figure 4(d). One of the limitations of the 2D catalyst morphology is the packing of material perpendicular to the flow of reactants and products, potentially resulting in increased mass transport resistances, Figure 4(d). This result highlights the need to find the balance between electronic and mass transport in PEMWE catalyst layers. One of the remaining hurdles to wide-spread integration of PEMWE is the scarcity and high cost of Ir; Ir is one of the least abundant elements on earth with a global annual production of only 7.25 tonnes⁶. Addressing Ir scarcity and the HCD losses observed for the npIr_x-NS, we demonstrate the ability of the npIr_x-NS electrocatalyst to perform at ultra-low loadings (0.06 mg_{Ir} cm⁻²), **Figure 5**. Polarization performance for the npIr_x-NS at this loading is comparable to that for TKK IrO₂, Figure 5(a). There is also no loss in performance for the npIr_x-NS when decreasing the loading from 0.17 mg_{lr} cm⁻² to 0.06 mg_{lr} cm⁻², Figure 5(d). In Figure 5(b), the lower anode

loading alleviates the high mass transport resistance for the npIr_x-NS. This is due to the reduction in stacking of the 2D nanosheets and an overall reduction in the thickness of the catalyst layer. However, we argue that it is the partial stacking and lateral interaction between the nanosheets, along with the metallic backbone of the nanoporous structure, that lead to reductions in ohmic overpotential at HCD, **Figure 5(c)**. The proportional decrease in ohmic overpotential for the npIr_x-NS over the TKK IrO₂ increases when moving from the 0.17 to the 0.06 mg_{Ir} cm⁻² loading (50 mV at 2.4 A/cm²), comparing **Figures 4(c)** and **5(c)**. At lower anode loadings, traditional nanoparticulate-based catalysts, particularly those that are unsupported, can have incomplete contact with the gas diffusion media and hence large fractions of catalytic material can be disconnected, **Figure 1(c)**. The sheet morphology of the npIr_x-NS helps to maintain lateral contact between the catalyst even at low loadings, increasing the proportion of catalyst material that is in electrical contact with the current collector.

The demonstrated ability of the npIr_x-NS to operate at loadings as low as 0.06 mg_{Ir} cm⁻² puts them in a rare class of materials with the capability to perform in a PEMWE at such low loadings. The npIr_x-NS performance at ultra-low loadings is particularly striking when compared to a commercial catalyst-coated membrane (CCM) that has been evaluated through a collaboration between a number of different research groups/labs⁵¹, **Figure 5(a)**. However, stability is equally if not more important. It has been demonstrated that at ultra-low loadings, IrO₂ exhibits poor durability under various accelerated stress test (AST) protocols^{52,53}. These foundational works on electrolysis ASTs have demonstrated that lower potential limits (LPL) affect Ir dissolution through reduction of surface Ir oxides and upper potential limits (UPL) affect the degree of surface oxidation, both effects are exasperated at low and ultra-low loadings. In order to assess and isolate durability of the npIr_x-NS in the PEMWE at both low and ultra-low loadings, we choose a LPL of

1.3 V and UPLs of 1.8 and 2.0 V for the ultra-low (0.06 mg_{Ir} cm⁻²) and low loaded (0.17 mg_{Ir} cm⁻²) ²) npIr_x-NS MEAs respectively (scan rate of 100 mV/s for 50,000 cycles). We note that the number of AST cycles here far exceeds those in other recent published work 15,52,53. At low loadings, Figure 6(a) shows that following 50,000 AST cycles, there is only a small drop in performance at low current densities (LCD), but there is a significant improvement at HCD. A similar degree of stability is observed at ultra-low loadings, Figure 5(d). This HCD performance improvement during AST has not been observed previously with other catalysts^{52,54}. We hypothesize that it is tied to a potential-induced structural reorganization of the nanoporous architecture. The double layer capacitance, extracted from CVs (Figures S3 and S4), during the progression of the AST is plotted in Figure 6(c). The observed increase in double layer capacitance during AST is potentially an indication of a gradual increase in the accessibility of the internal porosity of the npIr_x-NS, increasing the ECSA of the material and mitigating the mass transport losses observed at beginning of life (BOL). Figure 6(b) shows that there is a significant improvement in the mass transport overpotential at end of life (EOL). This also suggests an increase in accessibility within the catalyst layer.

To probe this further, we perform ex-situ characterization of the low loaded MEA. Comparing the TEM micrographs of the npIr_x-NS at BOL and EOL, a general increase in porosity is observed, as evidenced by the decrease in the "density" of the porous structure, **Figure 7**. Qualitative analysis of the high-resolution TEM images, top and bottom images on the right of **Figure 7**, potentially indicate a reduction in the total surface coverage of the disordered amorphous oxide, converting it to a more ordered crystalline oxide. The disordered amorphous oxide on the surface of the npIr_x-NS at BOL is characteristic of the atomic-scale morphology post-dealloying^{46,55}. However, following dealloying, while the surface is passivated with a thin

amorphous oxide, the bulk of the structure remains metallic. The general fingerprint features in the CVs during AST, Figure S3, indicate a transition from a nominally metallic Ir at BOL, in line with the BOL XPS (Figure S5), to a state that is more consistent with higher valent Ir species, presenting peaks that can be associated with Ir(III) – Ir(IV) and Ir(IV) – Ir(>IV)⁵⁶. This change in material chemistry/stoichiometry can also affect the wettability of the nanoporous catalyst surface, which could directly impact the mass transport properties of the material. Taken together, the opening of the porosity and change in the chemistry/stoichiometry of the catalyst surface during AST is the likely source of the high current density performance improvement. The structural/compositional evolution of the npIr_x-NS caused by the AST is further analyzed using small-angle and wide-angle X-ray scattering (SAXS/WAXS), conducted at the Advanced Photon Source at Argonne National Laboratory. Comparing BOL (fresh) to EOL, the WAXS data, Figure S6, indicates that a crystalline Ir oxide is formed during AST cycling. The bimodal nature of the WAXS peaks after AST cycling also indicate that a crystalline Ir phase co-exists with the Ir oxide phase. This corresponds well with both the TEM (Figure 7) and CV (Figure S3) data. The conversion of the surface of the npIrx-NS from a disordered amorphous oxide to a more ordered crystalline oxide is one potential source for the slight drop in performance at LCD following AST, Figure 6(a). The volume fraction distribution, Figure S6(c), also indicates a general reduction in average particle size following AST. This is potentially related to the opening of the porosity, shifting the average characteristic length scale of the system toward that of the nanosheet porosity. The lattice spacing, as measured from the TEM images, for both BOL and EOL are estimated to be 0.2353 nm. If the entirety of the nanoporous structure were to convert from a metallic Ir to a crystalline oxide, we would expect some change in the average lattice spacing, as determined from TEM images. Combined with the XPS and the X-ray scattering data, this is an indication that the metallic backbone of the npIr_x-NS remains metallic following AST, while the surface converts to an ordered crystalline Ir oxide. The general conclusion that can be drawn from the AST analysis is that the npIr_x-NS, even at ultra-low loadings, are an incredibly stable catalyst material that shows great promise for use in commercial PEMWEs.

Conclusions

In summary, we demonstrate a new top-down electrochemical processing technique to synthesize nanoporous Ir nanosheets (npIr_x-NS) from a homogeneous Ni-Ir alloy precursor. The average pore size of 5-10 nm, sheet thickness between 60 and 100 nm, and lateral dimensions of 1 – 2 μm make these ideal electrode materials for acidic OER in PEMWE. Voltage breakdown analysis of the PEMWE polarization curves demonstrates that initial performance losses due to mass transport limitations for the npIr_x-NS are mitigated through potential induced restructuring of the nanoporous nanosheets, improving catalyst accessibility and decreasing the mass transport overpotential to levels comparable to that observed for an anode using a commercial standard TKK IrO₂ catalyst. The true advantage of the nanoporous nanosheet morphology is observed at ultralow Ir anode loadings, 0.06 mg_{Ir} cm⁻², where the combination of lateral connectivity and interconnected metallic backbone of the nanoporous metal yield significant decreases to HCD ohmic losses. The npIr_x-NS also exhibits stable performance over 50,000 AST cycles in the PEMWE. As a result of a unique balance of conductive internal metallic structure, high aspect ratio, and stable morphology, the npIr_x-NS are a promising material for next generation PEMWEs.

Acknowledgements

J.S. and S.C. acknowledge funding from the National Science Foundation Division of Materials Research under award number 1904571. X.P. and N.D. would like to acknowledge the Department of Energy – Office of Energy Efficiency and Renewable Energy – Hydrogen and Fuel Cell Technologies Office (DOE-EERE-HFTO) under Contract Number DE-AC02-05CH11231. D.M. and N.K. work at Argonne National Laboratory is supported by the U.S. Department of Energy, Office of Energy Efficiency, Hydrogen and Fuel Cell Technologies Office under contract DE-AC02-06CH11357. X.P. and N.D. would also like to thank Chenyu Song from the National Center for Electron Microscopy (NCEM) for the support of transmission electron microscopy. Use of the Advanced Photon Source (APS), an Office of Science user facility operated by Argonne National Laboratory, is supported by the U.S. Department of Energy, Office of Science, Office of Basic Energy Sciences, under Contract No. DE-AS02-06CH11357. The authors would like to thank Jan Ilavsky and Ivan Kuzmenko of the X-ray Science Division, beamline 9-ID, of the APS.

Conflict of Interest

The authors declare no conflict of interest

Author Contributions

S.C. performed the synthesis and half-cell measurements under the guidance of J.S. X.P. performed the MEA fabrication, testing and analysis under the guidance of N.D. G.Z. performed the XPS measurement. N.K. performed the X-ray scattering experiment under the guidance of D.M. The manuscript was written through contribution of all authors. S.C. and X.P. contributed equally to this work.

References:

- 1. Pivovar, B., Rustagi, N., Satyapal, S. Hydrogen at scale (H2@scale): key to a clean, economic, and sustainable energy system. *Electrochem. Soc. Interface* **27**, 47–52 (2018).
- 2. Department of Energy Hydrogen Program Plan. https://www.hydrogen.energy.gov/pdfs/hydrogen-prog (2020).
- 3. Hydrogen strategy for Canada: Seizing the Opportunities for Growth. https://www.nrcan.gc.ca/sites/www.nrcan.gc.ca/file (2020).
- 4. *Hydrogen Roadmap Europe: A sustainable pathway for the european energy transition.* (2019). doi:10.2843/249013
- 5. Ayers, K., Danilovic, N., Ouimet, R., Carmo, M., Pivovar, B. & Bornstein, M. Perspectives on low-temperature electrolysis and potential for renewable hydrogen at scale. *Annu. Rev. Chem. Biomol. Eng.* **10**, 219–239 (2019).
- 6. Taie, Z., Peng, X., Kulkarni, D., Zenyuk, I. V., Weber, A. Z., Hagen, C. & Danilovic, N. Pathway to Complete Energy Sector Decarbonization with Available Iridium Resources using Ultralow Loaded Water Electrolyzers. *ACS Appl. Mater. Interfaces* **12**, 52701–

- 52712 (2020).
- 7. Danilovic, Nemanja, Subbaraman, Ramachandran, Chang, Kee Chul, Chang, Seo Hyoung, Kang, Yijin J., Snyder, Joshua, Paulikas, Arvydas P., Strmcnik, Dusan, Kim, Yong Tae, Myers, Deborah, Stamenkovic, Vojislav R., Markovic, N. M. Activity-stability trends for the oxygen evolution reaction on monometallic oxides in acidic environments. *J. Phys. Chem. Lett.* **5**, 2474–2478 (2014).
- 8. Kasian, O., Geiger, S., Li, T., Grote, J. P., Schweinar, K., Zhang, S., Scheu, C., Raabe, D., Cherevko, S., Gault, B. & Mayrhofer, K. J. J. Degradation of iridium oxides via oxygen evolution from the lattice: Correlating atomic scale structure with reaction mechanisms. *Energy Environ. Sci.* **12**, 3548–3555 (2019).
- 9. Seitz, L. C., Dickens, C. F., Nishio, K., Hikita, Y., Montoya, J., Doyle, A., Kirk, C., Vojvodic, A., Hwang, H. Y., Norskov, J. K. & Jaramillo, T. F. A highly active and stable IrO x /SrIrO 3 catalyst for the oxygen evolution reaction. *Science (80-.).* **353**, 1011–1014 (2016).
- 10. Diaz-Morales, O., Raaijman, S., Kortlever, R., Kooyman, P. J., Wezendonk, T., Gascon, J., Fu, W. T. & Koper, M. T. M. Iridium-based double perovskites for efficient water oxidation in acid media. *Nat. Commun.* 7, 12363 (2016).
- 11. Kim, Y.-T., Lopes, P. P., Park, S.-A., Lee, A.-Y., Lim, J., Lee, H., Back, S., Jung, Y., Danilovic, N., Stamenkovic, V., Erlebacher, J., Snyder, J. & Markovic, N. M. Balancing activity, stability and conductivity of nanoporous core-shell iridium/iridium oxide oxygen evolution catalysts. *Nat. Commun.* **8**, 1449 (2017).
- 12. Alia, S. M., Rasimick, B., Ngo, C., Neyerlin, K. C., Kocha, S. S., Pylypenko, S., Xu, H. & Pivovar, B. S. Activity and Durability of Iridium Nanoparticles in the Oxygen Evolution Reaction. *J. Electrochem. Soc.* **163**, F3105–F3112 (2016).
- 13. Mandal, M., Moore, M. & Secanell, M. Measurement of the Protonic and Electronic Conductivities of PEM Water Electrolyzer Electrodes. *ACS Appl. Mater. Interfaces* 12, 49549–49562 (2020).
- 14. Regmi, Y. N., Tzanetopoulos, E., Zeng, G., Peng, X., Kushner, D. I., Kistler, T. A., King, L. A. & Danilovic, N. Supported Oxygen Evolution Catalysts by Design: Toward Lower Precious Metal Loading and Improved Conductivity in Proton Exchange Membrane Water Electrolyzers. *ACS Catal.* **10**, 13125–13135 (2020).
- 15. Hegge, F., Lombeck, F., Cruz Ortiz, E., Bohn, L., von Holst, M., Kroschel, M., Hübner, J., Breitwieser, M., Strasser, P. & Vierrath, S. Efficient and Stable Low Iridium Loaded Anodes for PEM Water Electrolysis Made Possible by Nanofiber Interlayers. *ACS Appl. Energy Mater.* **3**, 8276–8284 (2020).
- 16. Alia, S. M., Shulda, S., Ngo, C., Pylypenko, S. & Pivovar, B. S. Iridium-Based Nanowires as Highly Active, Oxygen Evolution Reaction Electrocatalysts. *ACS Catal.* **8**, 2111–2120 (2018).
- 17. Schuler, T., Ciccone, J. M., Krentscher, B., Marone, F., Peter, C., Schmidt, T. J. & Büchi, F. N. Hierarchically Structured Porous Transport Layers for Polymer Electrolyte Water

- Electrolysis. Adv. Energy Mater. 10, 1903216 (2020).
- 18. Schuler, T., Schmidt, T. J. & Büchi, F. N. Polymer Electrolyte Water Electrolysis: Correlating Performance and Porous Transport Layer Structure: Part II. Electrochemical Performance Analysis. *J. Electrochem. Soc.* **166**, F555–F565 (2019).
- 19. Zhao, S., Stocks, A., Rasimick, B., More, K. & Xu, H. Highly Active, Durable Dispersed Iridium Nanocatalysts for PEM Water Electrolyzers. *J. Electrochem. Soc.* **165**, F82–F89 (2018).
- 20. Karimi, F., Bazylak, A. & Peppley, B. A. Effect of Calcination Temperature on the Morphological and Electrochemical Characteristics of Supported Iridium Hydroxyoxide Electrocatalysts for the PEM Electrolyzer Anode. *J. Electrochem. Soc.* **164**, F464–F474 (2017).
- 21. Zhao, Y., Luo, M., Chu, S., Peng, M., Liu, B., Wu, Q., Liu, P., de Groot, F. M. F. & Tan, Y. 3D nanoporous iridium-based alloy microwires for efficient oxygen evolution in acidic media. *Nano Energy* **59**, 146–153 (2019).
- 22. Kim, Y. T., Lopes, P. P., Park, S. A., Lee, A. Y., Lim, J., Lee, H., Back, S., Jung, Y., Danilovic, N., Stamenkovic, V., Erlebacher, J., Snyder, J. & Markovic, N. M. Balancing activity, stability and conductivity of nanoporous core-shell iridium/iridium oxide oxygen evolution catalysts. *Nat. Commun.* **8**, 1449 (2017).
- 23. Qiu, H.-J., Fang, G., Gao, J., Wen, Y., Lv, J., Li, H., Xie, G., Liu, X. & Sun, S. Noble Metal-Free Nanoporous High-Entropy Alloys as Highly Efficient Electrocatalysts for Oxygen Evolution Reaction. *ACS Mater. Lett.* **1,** 526–533 (2019).
- 24. Cui, X., Zhang, B., Zeng, C., Wen, H., Guo, S. Monolithic nanoporous Ni-Fe alloy by dealloying laser processed Ni-Fe-Al as electrocatalyst toward oxygen evolution reaction. *Int. J. Hydrogen Energy* **43**, 15234–15244 (2018).
- 25. Chatterjee, S., Intikhab, S., Profitt, L., Li, Y., Natu, V., Gawas, R. & Snyder, J. Nanoporous multimetallic Ir alloys as efficient and stable electrocatalysts for acidic oxygen evolution reactions. *J. Catal.* **393**, 303–312 (2021).
- 26. Li, R. & Sieradzki, K. Ductile-brittle transition in random porous Au. *Phys. Rev. Lett.* **68**, 1168–1171 (1992).
- 27. Biener, J., Hodge, A. M. & Hamza, A. V. Microscopic failure behavior of nanoporous gold. *Appl. Phys. Lett.* **87**, 121908 (2005).
- 28. Ilavsky, J., Jemina, P., Allen, A., Zhang, F., Levine, L., Long, G. Ultra-small-angle X-ray scattering at the Advanced Photon Source. *J. Appl. Cryst.* **42**, 469–479 (2009).
- 29. Ilavsky, J. Nika: software for two-dimensional data reduction. *J. Appl. Cryst.* **45**, 324–328 (2012).
- 30. Ilavsky, J., Jemian, P. Irena: tool suite for modeling and analysis of small-angle scattering. *J. Appl. Cryst.* **42**, 347–353 (2009).
- 31. Jemian, P., Weertman, J., Long, G., Spal, R. Characterization of 9Cr-1MoVNb steel by

- anomalous small-angle X-ray scattering. Acta Metall. Mater. 39, 2477–2487 (1991).
- 32. Bratsch, S. G. Standard Electrode Potentials and Temperature Coefficients in Water at 298.15 K. *J. Phys. Chem. Ref. Data* (1989). doi:10.1063/1.555839
- 33. Yang, G., Yu, S., Li, Y., Li, K., Ding, L., Xie, Z., Wang, W. & Zhang, F. Y. Role of electron pathway in dimensionally increasing water splitting reaction sites in liquid electrolytes. *Electrochim. Acta* **362**, 137113 (2020).
- 34. Mo, J., Kang, Z., Yang, G., Li, Y., Retterer, S. T., Cullen, D. A., Toops, T. J., Bender, G., Pivovar, B. S., Green, J. B. & Zhang, F. Y. In situ investigation on ultrafast oxygen evolution reactions of water splitting in proton exchange membrane electrolyzer cells. *J. Mater. Chem. A* 5, 18469–18475 (2017).
- 35. Erlebacher, J. An Atomistic Description of Dealloying. *J. Electrochem. Soc.* **151,** C614–C626 (2004).
- 36. Erlebacher, J., Aziz, M. J., Karma, A., Dimitrov, N. & Sieradzki, K. Evolution of nanoporosity in dealloying. *Nature* **410**, 450–453 (2001).
- 37. Sieradzki, K., Dimitrov, N., Movrin, D., McCall, C., Vasiljevic, N., Erlebacher, J. The Dealloying Critical Potential. *J. Electrochem. Soc.* **149**, B370–B377 (2002).
- 38. Fujita, T., Guan, P., McKenna, K., Lang, X., Hirata, A., Zhang, L., Tokunaga, T., Arai, s., Yamamoto, Y., Tanaka, N., Ishikawa, Y., Asao, N., Yamamoto, Y., Erlebacher, J., Chen, M. Atomic origins of the high catalytic activity of nanoporous gold. *Nat. Mater.* 11, 775–780 (2012).
- 39. Danilovic, N., Subbaraman, R., Chang, K. C., Chang, S. H., Kang, Y., Snyder, J., Paulikas, A. P., Strmcnik, D., Kim, Y. T., Myers, D., Stamenkovic, V. R. & Markovic, N. M. Using surface segregation to design stable Ru-Ir oxides for the oxygen evolution reaction in acidic environments. *Angew. Chemie Int. Ed.* **53**, 14016–14021 (2014).
- 40. Snyder, J., Fujita, T., Chen, M., Erlebacher, J. Oxygen reduction in nanoporous metalionic liquid composite electrocatalysts. *Nat. Mater.* **9**, 904–907 (2010).
- 41. Sun, C. Q., Wang, Y., Tay, B. K., Li, S., Huang, H. & Zhang, Y. B. Correlation between the melting point of a nanosolid and the cohesive energy of a surface atom. *J. Phys. Chem. B* **106**, 10701–10705 (2002).
- 42. Renner, F. U., Stierle, A., Dosch, H., Kolb, D. M. & Zegenhagen, J. The influence of chloride on the initial anodic dissolution of Cu3Au(111). *Electrochem. commun.* **9,** 1639–1642 (2007).
- 43. Ankah, G. N., Pareek, A., Cherevko, S., Topalov, A. A., Rohwerder, M. & Renner, F. U. The influence of halides on the initial selective dissolution of Cu3Au (111). *Electrochim. Acta* **85**, 384–392 (2012).
- 44. Zhang, Z., Zhang, C., Sun, J. & Kou, T. Influence of anion species on electrochemical dealloying of single-phase Al2Au alloy in sodium halide solutions. *RSC Adv.* **2**, 4481 (2012).

- 45. Snyder, J., Asanithi, P., Dalton, A., Erlebacher, J. Stabilized Nanoporous Metals by Dealloying Ternary Alloy Precursors. *Adv. Mater.* **20**, 4883–4886 (2008).
- 46. Snyder, J., Livi, K. & Erlebacher, J. Dealloying Silver/Gold Alloys in Neutral Silver Nitrate Solution: Porosity Evolution, Surface Composition, and Surface Oxides. *J. Electrochem. Soc.* **155**, C464 (2008).
- 47. Peng, X., Taie, Z., Liu, J., Zhang, Y., Peng, X., Regmi, Y. N., Fornaciari, J. C., Capuano, C., Binny, D., Kariuki, N. N., Myers, D. J., Scott, M. C., Weber, A. Z. & Danilovic, N. Hierarchical electrode design of highly efficient and stable unitized regenerative fuel cells (URFCs) for long-term energy storage. *Energy Environ. Sci.* 13, 4872–4881 (2020).
- 48. Soboleva, T., Zhao, X., Malek, K., Xie, Z., Navessin, T. & Holdcroft, S. On the micro-, meso-, and macroporous structures of polymer electrolyte membrane fuel cell catalyst layers. *ACS Appl. Mater. Interfaces* **2**, 375–384 (2010).
- 49. Alia, S. M. & Anderson, G. C. Iridium Oxygen Evolution Activity and Durability Baselines in Rotating Disk Electrode Half-Cells. *J. Electrochem. Soc.* **166**, F282–F294 (2019).
- 50. Regmi, Y. N., Peng, X., Fornaciari, J. C., Wei, M., Myers, D. J., Weber, A. Z. & Danilovic, N. A low temperature unitized regenerative fuel cell realizing 60% round trip efficiency and 10 000 cycles of durability for energy storage applications. *Energy Environ. Sci.* (2020). doi:10.1039/c9ee03626a
- 51. Bender, G., Carmo, M., Smolinka, T., Gago, A., Danilovic, N., Mueller, M., Ganci, F., Fallisch, A., Lettenmeier, P., Friedrich, K. A., Ayers, K., Pivovar, B., Mergel, J. & Stolten, D. Initial approaches in benchmarking and round robin testing for proton exchange membrane water electrolyzers. *Int. J. Hydrogen Energy* **44**, 9174–9187 (2019).
- 52. Alia, S. M., Soc, J. E., Alia, S. M., Stariha, S. & Borup, R. L. Electrolyzer Durability at Low Catalyst Loading and with Dynamic Operation. *J. Ele* **15**, F1164–F1172 (2019).
- 53. Weiß, A., Siebel, A., Bernt, M., Shen, T.-H., Tileli, V. & Gasteiger, H. A. Impact of Intermittent Operation on Lifetime and Performance of a PEM Water Electrolyzer. *J. Electrochem. Soc.* **166**, F487–F497 (2019).
- 54. Alia, S. *H2@Scale*: Experimental Characterization of Durability of Advanced Electrolyzer Concepts in Dynamic Loading. (2019).
- 55. Pareek, A., Borodin, S., Bashir, A., Ankah, G. N., Keil, P., Eckstein, G. A., Rohwerder, M., Stratmann, M., Gründer, Y. & Renner, F. U. Initiation and inhibition of dealloying of single crystalline Cu 3Au (111) surfaces. *J. Am. Chem. Soc.* **133**, 18264–18271 (2011).
- 56. Minguzzi, A., Locatelli, C., Cappelletti, G., Scavini, M., Vertova, A., Ghigna, P. & Rondinini, S. IrO2-Based Disperse-Phase Electrocatalysts: A Complementary Study by Means of the Cavity-Microelectrode and Ex-Situ X-ray Absorption Spectroscopy. *J. Phys. Chem. A* **116**, 6497–6504 (2012).

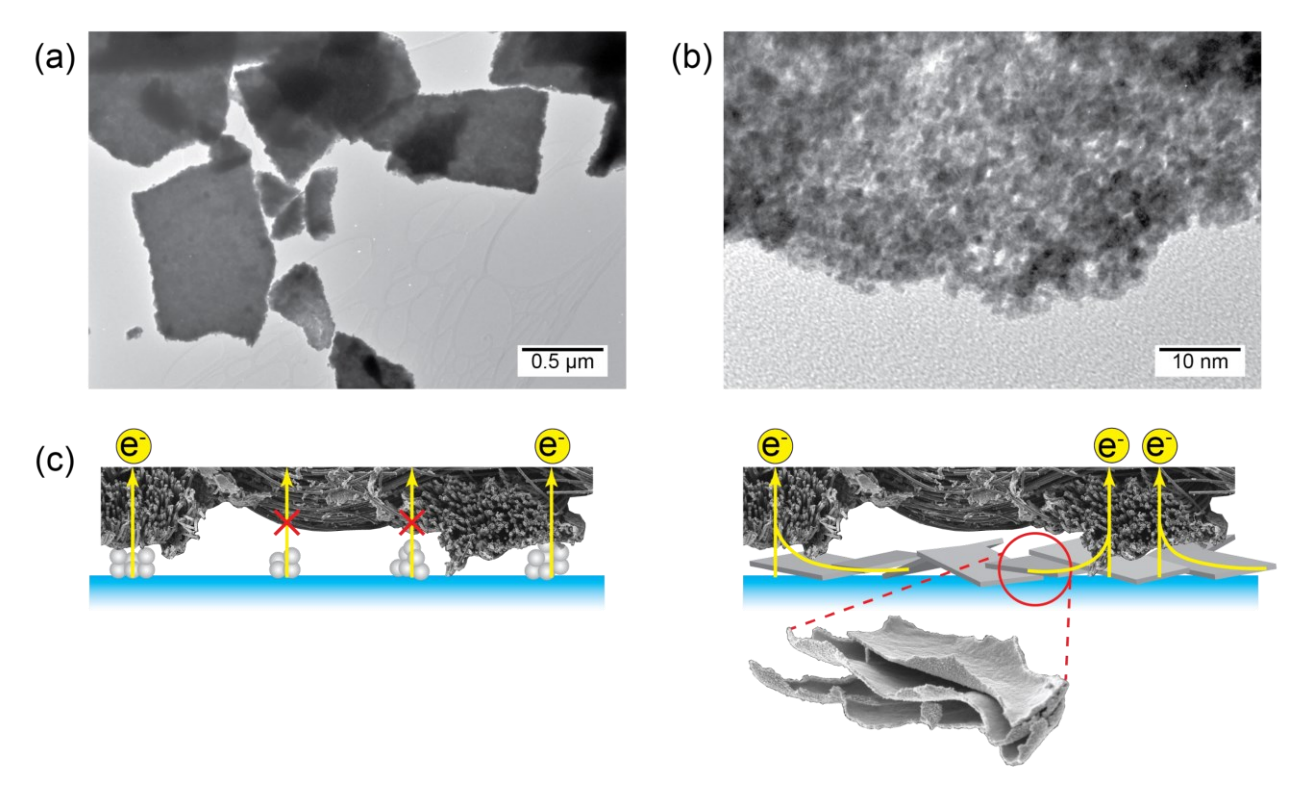


Figure 1: (a) and (b) TEM micrographs of npIr_x-NS formed through dealloying of a Ni₉₅Ir₅ precursor alloy. (c) Schematic representation of (left) traditional nanoparticulate PEMWE anode catalyst aggregation and interaction with the gas diffusion layer (GDL) and (right) lateral connectivity of the npIr_x-NS provides a minimally resistive pathway for electron conduction from the catalyst to the GDL and eventually the current collector.

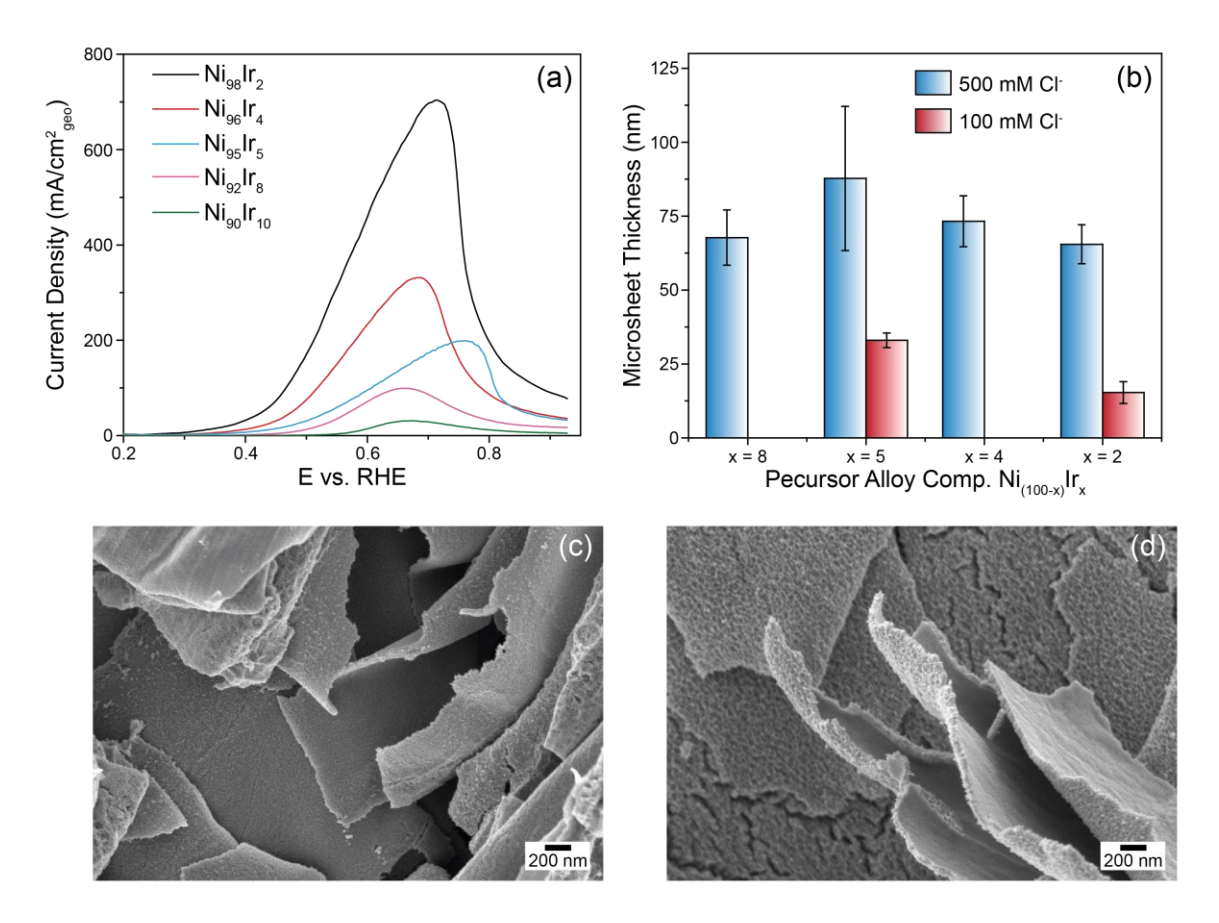


Figure 2: (a) Anodic sweep potentiodynamic dealloying current densities in 2 M $H_2SO_4 + 0.5$ M HCl for various precursor $Ni_{(100-x)}Ir_x$ alloys. (b) Nanosheet thickness as a function of precursor alloy composition and chloride content in the dealloying electrolyte. SEM micrographs of npIr_x-NS from (c) $Ni_{92}Ir_8$ and (b) $Ni_{95}Ir_5$ dealloyed in 2 M $H_2SO_4 + 0.5$ M HCl.

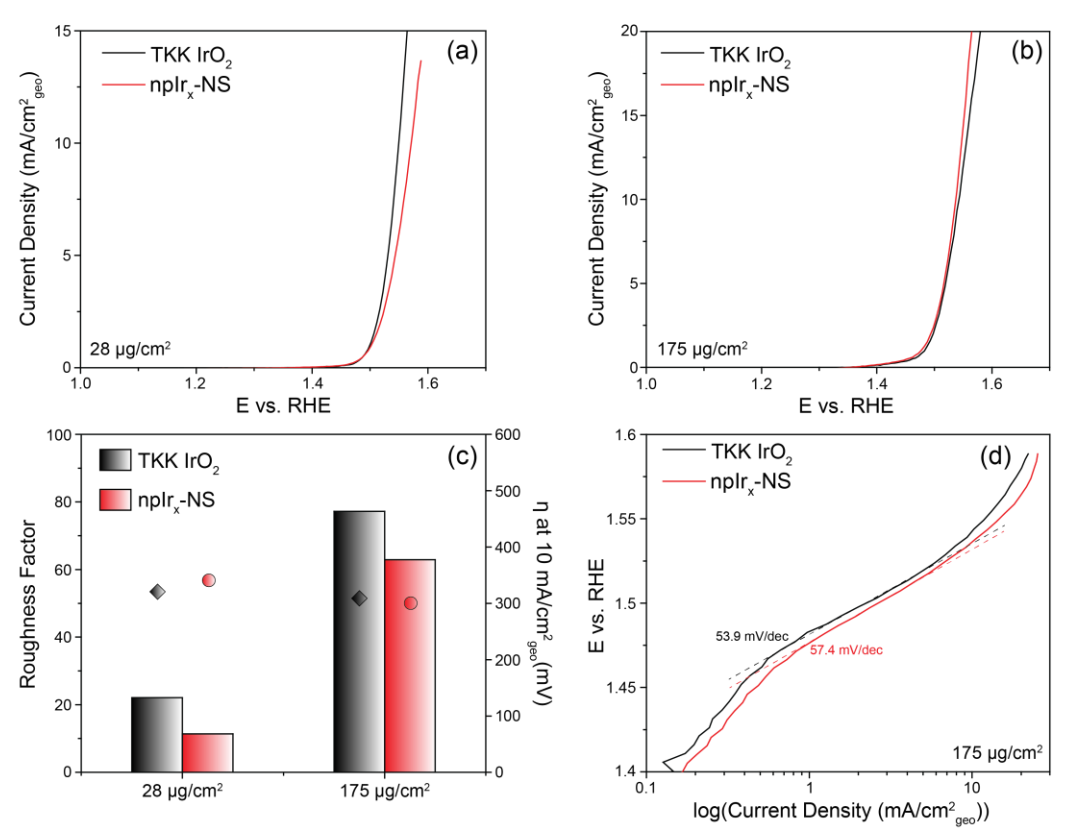


Figure 3: (a) RDE OER polarization curves in 0.1 M HClO₄ for TKK IrO₂ (black) and npIr_x-NS (red) with a catalyst loading of 28 μ g/cm². (b) RDE OER polarization curves in 0.1 M HClO₄ for TKK IrO₂ (black) and npIr_x-NS (red) with a catalyst loading of 175 μ g/cm². (c) Roughness factors (RF) for TKK IrO₂ (black) and npIr_x-NS (red) at 28 μ g/cm² and 175 μ g/cm² loading and the corresponding OER overpotential (symbols; right axis). (d) OER Tafel plots, including Tafel slopes for TKK IrO₂ (black) and npIr_x-NS (red) at 175 μ g/cm² loading.

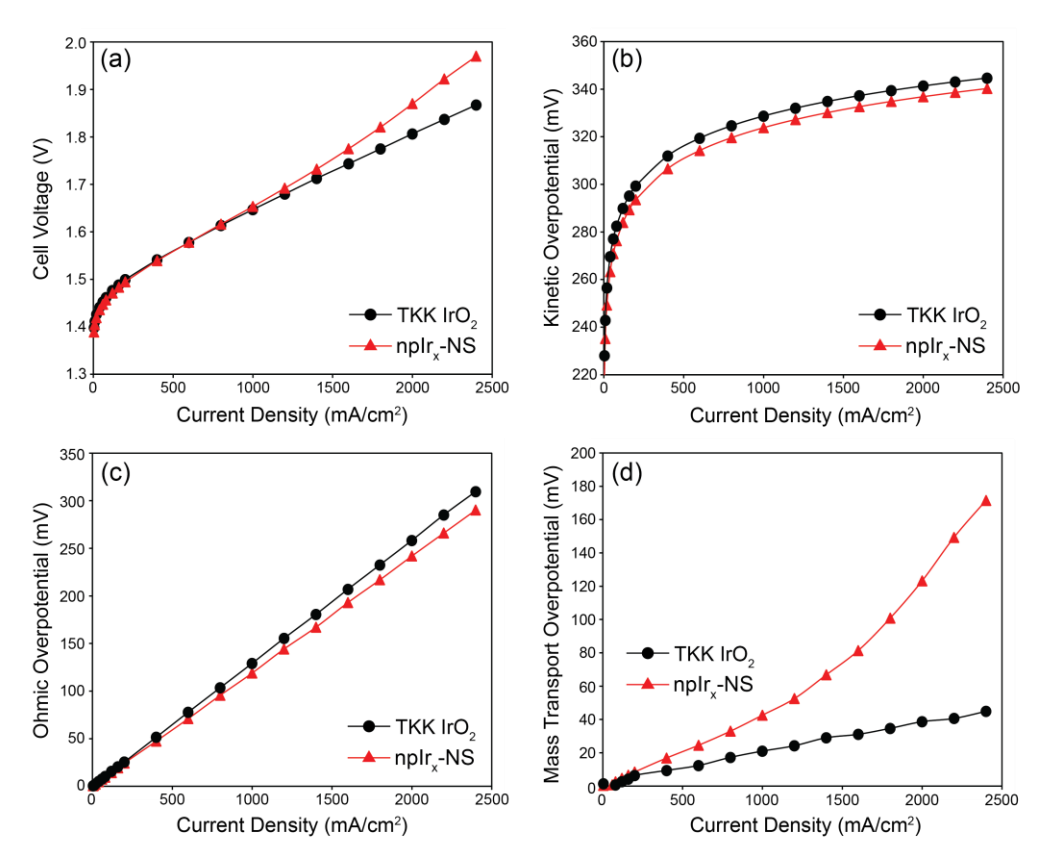


Figure 4: Polarization performance voltage breakdown for npIr_x-NS and TKK IrO₂ at beginning of life (BOL): (a) polarization curves, (b) kinetic overpotential, (c) ohmic overpotential, and (d) mass transport overpotential as a function of geometric current density. Anode Ir loading is 0.17 mg_{Ir} cm⁻² for both MEAs.

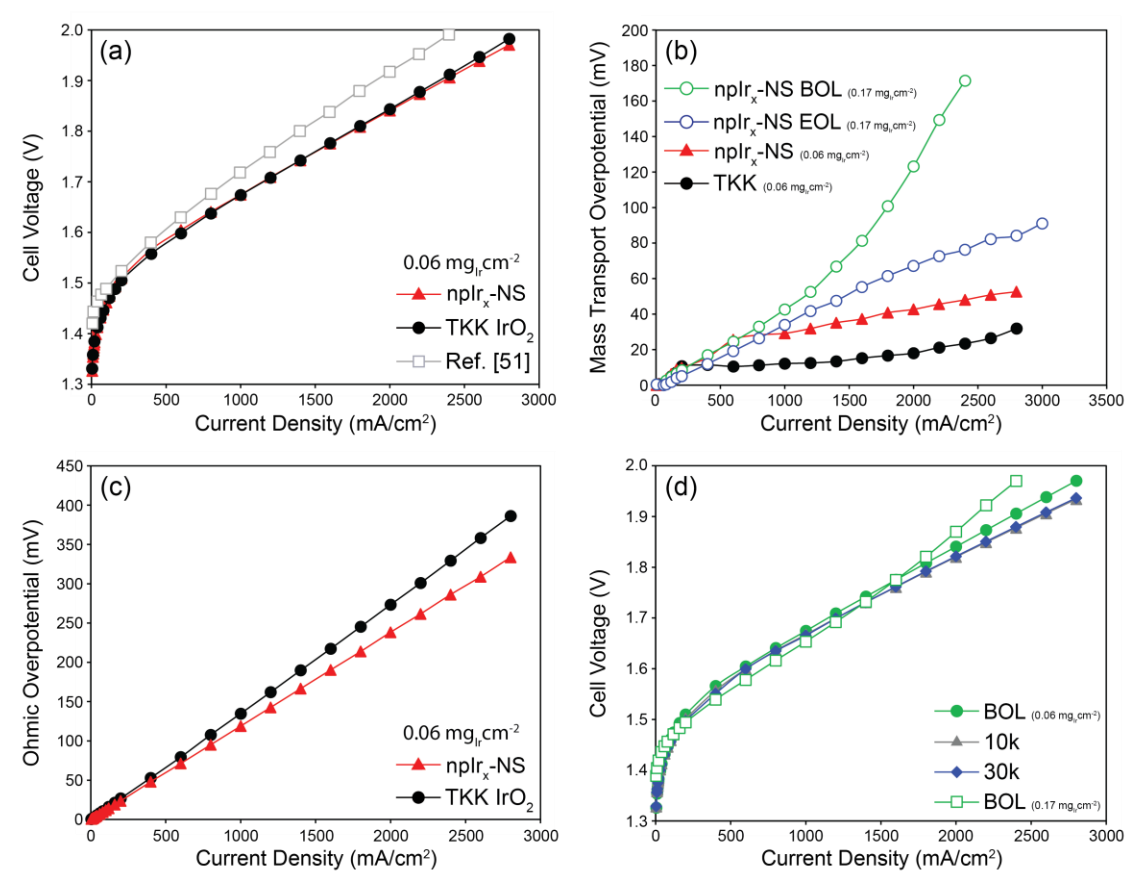


Figure 5: (a) Polarization curves for npIr_x-NS (red) and TKK IrO₂ (black) at 0.06 mg_{Ir} cm⁻² anode loading. Included for comparison is a representative polarization curve (grey) from the round robin study completed using a commercially available catalyst coated membrane (CCM) tested at a range of facilities by a group of participating researchers⁵¹. Anode loading on this CCM is 2.5 mg_{Ir} cm⁻². (b) Mass transport overpotential for 0.17 mg_{Ir} cm⁻² anode loading for npIr_x-NS BOL (open green) and EOL (open blue) in comparison to BOL npIr_x-NS (red) and TKK IrO₂ (black) at 0.06 mg_{Ir} cm⁻² anode loading. (c) Ohmic overpotential at BOL for npIr_x-NS (red) and TKK IrO₂ (black) at 0.06 mg_{Ir} cm⁻² anode loading. We note that at low loadings for both the npIr_x-NS and TKK IrO₂, there is minimal change in all voltage breakdown plots from BOL to EOL. (d) Polarization curves for low anode loading npIr_x-NS (0.06 mg_{Ir} cm⁻²) at BOL (green closed), 10k (grey), and 30k (blue) AST cycles. The BOL polarization curve for npIr_x-NS at the higher anode loading (0.17 mg_{Ir} cm⁻²) (open green squares) is included for reference.

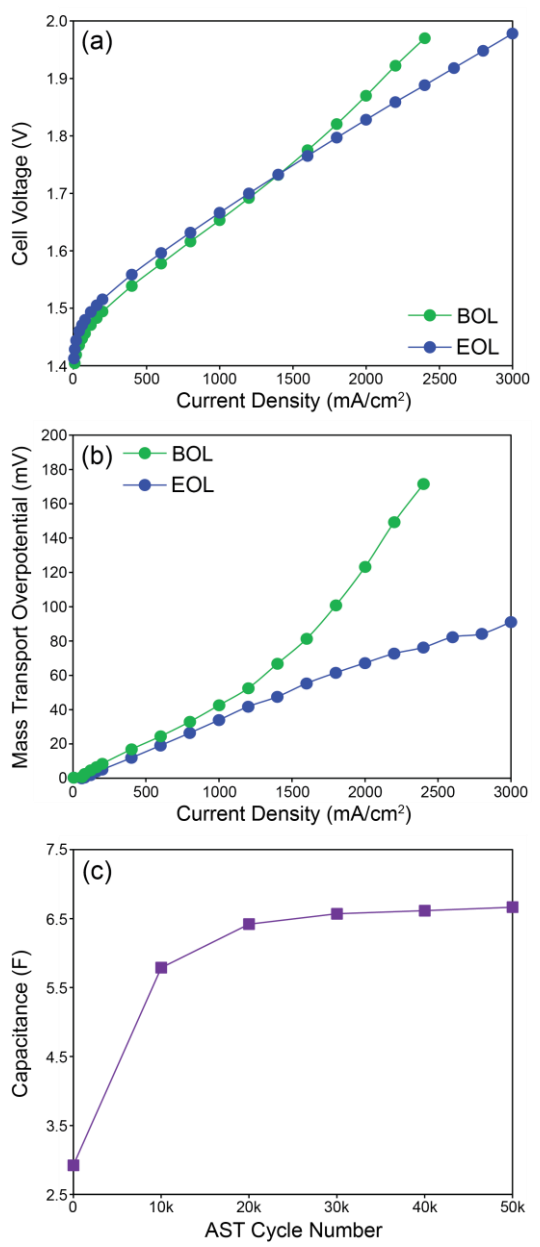


Figure 6: (a) Beginning of life (BOL) (green) and end of life (EOL) (blue) performance for the npIr_x-NS anode in a PEMWE; 50,000 AST cycles, anode Ir loading of 0.17 mg_{Ir} cm⁻². (b) Mass transport overpotential for the npIr_x-NS at BOL (green) and EOL (blue). (c) Pseudocapacitance of the npIr_x-NS catalyst layer as a function of AST cycle number; anode Ir loading of 0.17 mg_{Ir} cm⁻².

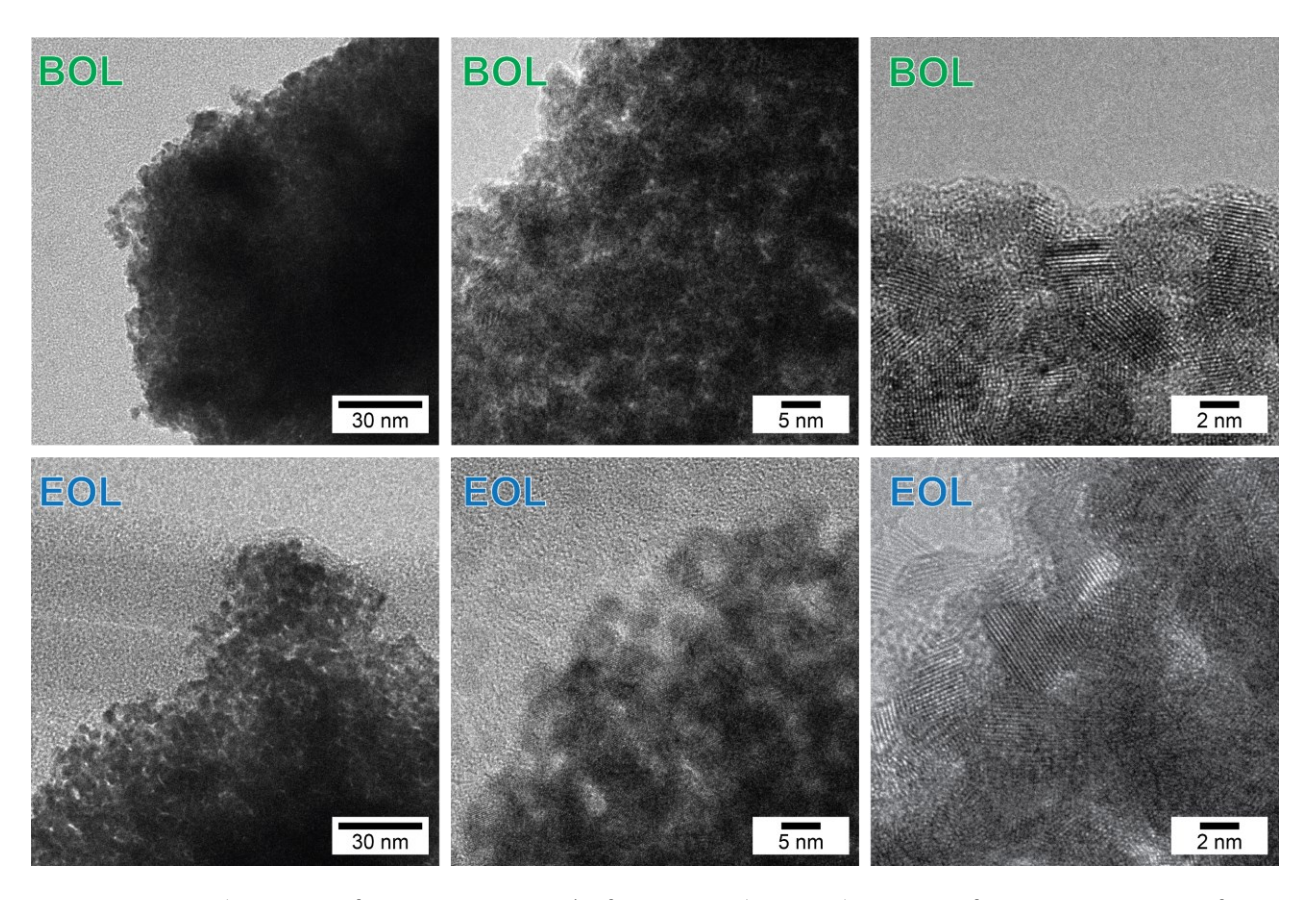


Figure 7: (Top) TEMs of BOL npIr_x-NS, before AST. (Bottom) TEMs of EOL np-Ir_x-NS, after AST; 50,000 AST cycles, 0.17 mg_{Ir} cm⁻² anode loading.